REVIEW

Importance of radiolytic reactions during high-LET irradiation modalities: LET effect, role of O$_2$ and radiosensitization by nanoparticles

Gérard Baldacchino[1*] , Emilie Brun[2], Ibtihel Denden[1], Sarah Bouhadoun[1], Raphael Roux[3], Hicham Khodja[3] and Cécile Sicard-Roselli[2]

*Correspondence:
gerard.baldacchino@cea.fr
[1] LIDYL, UMR9222 CEA,
CNRS, Université Paris-Saclay,
91191 Gif-sur-Yvette Cedex,
France
Full list of author information
is available at the end of the
article

Abstract

This article reviews radiation chemistry processes induced by high-linear energy transfer (LET) radiation. The first part gives a short historical introduction and defines the essential concepts of radiation chemistry. It is aimed at radiobiologists in search of basics in this discipline, to link to their biological observations. Then, special focus is done on LET effect, oxygen effect and nanoparticles as these parameters can influence the success of radiotherapy. The embraced point of view is the one from a chemist as involved molecular reactions in water are detailed and revealed, for example, how dioxygen can be produced in situ during high-LET irradiations, even in anoxic conditions. A step forward can be reached using nanoparticles in conjunction with radiation beams to enhance their effects. The last part of this review is thus devoted to the description of an original approach combining high-LET projectiles (3-MeV α-rays) and gold nanoparticles. Fluorescence microscopy was used to evaluate the formation yield of radicals in anoxic condition via scavenging by Ampliflu® Red. As with low-LET irradiations, an overproduction of radicals was obtained, encouraging to conduct a broader study and to consider nanoparticles in simulation as an additional source of radicals.

Keywords: Radiation chemistry, Linear energy transfer (LET) effect, Reactive oxygen species (ROS), Relative biological effectiveness (RBE), Oxygen enhancement ratio (OER), Radiosensitization, Gold nanoparticles (GNP)

Background

It is striking how chemists and biologists showed an interest for ionizing radiations very soon after their discovery by Roentgen and Becquerel, and initiated parallel developments of these new fields of research: radiation chemistry and radiobiology. Radiation chemistry deals with the chemical effects produced when materials are exposed to ionizing radiations and begun long before 1942 when it was formally named by Burton (Magee 1988). Early pioneering works were achieved by Curie and Debierne in 1901 by observing gas bubbling out of radium salt solutions, Giesel in 1902 (Giesel 1902), Ramsay in 1903, and the progress and enthusiasm persisted throughout the beginning of 20th century (Debierne 1914; Kernbaum 1909). Radiobiology and radiotherapy were at

stage without further delay with Grubbe who might be the first physician to use X-rays for therapeutic purpose in 1896 (News of Science 1957). An essential link between these subjects was underlying and in the 1920s', Fricke "recognized that the chemical effects of radiation should be studied to help understand the response of living systems to radiation, and in 1928 he established a laboratory to conduct such studies" (Zimbrick 2002). Radiation chemistry and radiobiology both benefited from improvements in technologies (accelerators, cyclotrons, lasers, new detectors, fast electronics, …): on the one hand to describe reactions at earlier chemical steps than those under human time-scale observations such as gas bubbling and stable molecules production (Kroh 1989; Wishart and Rao 2010; Hatano et al. 2011), on the other hand, to deploy new medical sources of irradiation. Many other details of the history of radiation chemistry are reported in the following reviews (Ferradini and Jay-Gerin 1999; Baldacchino 2017; Le Caer 2011).

The close intertwining between radiation chemistry and radiobiology is more newsworthy than ever. The increasing complexity of the questions addressed and techniques used by both fields comes along increasing specialization when an integrative description is needed. The aim of this review is to explicit the contribution of a chemist's point of view to the understanding of phenomenon induced by high-LET radiations. It is mainly intended for radiobiologists in search of basics in radiation chemistry, to link to their biological observations. We will mainly focus on deciphering the chemistry behind the ballistic effect and the oxygen effect, often mentioned as key advantages for such radiations. We will also discuss the use of extrinsic radiosensitizing agents such as nanoparticles to maximize the benefits of these irradiation modalities. To ease the comprehension for non-specialist readers, we will first introduce the essential concepts in radiation chemistry. As underlined by Jonah, "Almost all radiation chemists have been concerned at one time or another with aqueous radiation chemistry. It is the system that one must consider to understand the biological effects of radiation" (Jonah 1995), we will thus restrain our perimeter of interest to water.

Dose, LET and *G*-values

Particle-matter interaction is commonly depicted in time sequences starting at time "0" with the transfer of radiation energy to the substrate (physical phase) and "ending" with biological repercussions dozens of years after, if one considers carcinogenesis. Intermediately, chemical processes happen between the subpicosecond (10^{-12} s) and the millisecond.

Macroscopically speaking, the amount of energy absorbed in the sample is measured by the dose, D. $D = \mathrm{d}E/\mathrm{d}m$ where $\mathrm{d}E$ is the energy deposited by the radiation in a sample of mass $\mathrm{d}m$. In SI units, it is expressed in J kg^{-1} which is given the special name of gray (symbol Gy). But the absorbed energy is not uniformly distributed as the initial events are excitations and ionizations of the molecules along the trajectories of the particles present in the radiation beam or arising from it. To describe this non-homogeneous energy distribution, the notion of linear energy transfer (LET) was introduced. LET characterizes how the incident particles transfer their energy per unit distance. It is usually expressed in eV nm^{-1} or keV μm^{-1}. The vast majority of tabulated values of LET represents track-averaged LET: they are calculated by dividing the total deposited energy of an incident particle by its path length (i.e. track length), as defined in Chapter 13 in ref

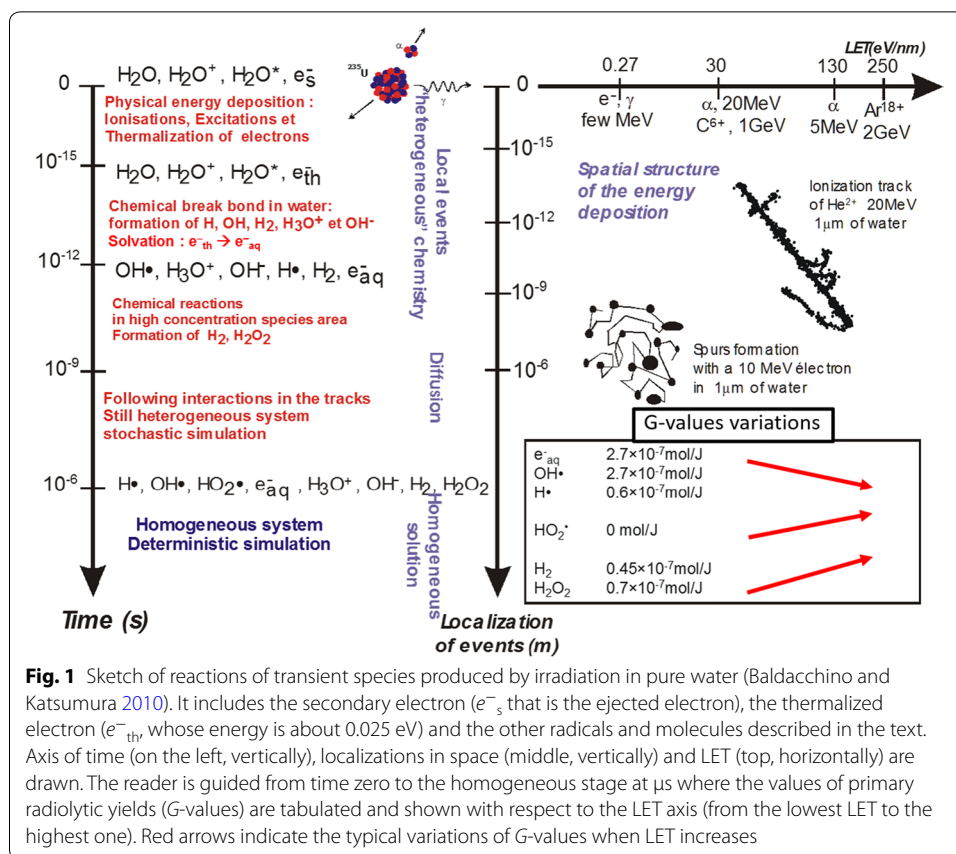Baldacchino *et al. Cancer Nano* (2019) 10:3

Page 3 of 21

(Hatano et al. 2011). While it can be convenient to get orders of magnitude and compare different radiation types, it ignores the important fact that LET changes as the particle slows down and so is not constant along the track.

Microscopically speaking, even the simplest radiolysis reactions involve a variety of reactive intermediates that react and disappear at different rates. For example, the physical interaction of energetic particles (γ-ray, X-ray, energetic electrons, α-ray, protons, ions) with water leads to discrete deposits of energy. Excited water (H_2O^*), $H_2O^{\cdot+}$ and the ejected electron (noted as e^-_s for secondary electron) are thus formed locally. In strongly polar solvents, like water, the geminate recombination of electrons with their positive parent cation is less favored, they become separated, which has a significant effect on the reactions taking place. Either they have enough energy to travel farther and they will form tracks on their own, or they slow down to reach thermic energies (around 25 meV, such an electron is noted e^-_{th}). If the ejected electrons have energy < 100 eV, their range are short and any subsequent ionization is produced close to the original ionization site, giving a small cluster of nanometer size, or "spur", of excited and ionized molecules. In the spurs, HO–H bond breaking occurs within a few 10 s of femtoseconds (10^{-15} s) to evacuate the excess energy deposited. ·OH, H·, H^+ and e^-_{th} are then considered as the first species formed during water radiolysis and chemistry starts with the neighboring network of water molecules, playing the roles of reactant and solvent by dipolar orientation in solvation processes. Solvation of e^-_{th} occurs within 10^{-12} s to form hydrated or aqueous electron (e^-_{aq}) (Farhataziz and Rodgers 1987). A diffusion step begins, from these areas of highly concentrated radicals, which is in competition with inter-radicals recombination. Table 1 gives the reaction rates of reactions occurring in this non-homogeneous kinetics stage.

Therefore, the result of the competition between recombination and diffusion strongly depends on how the energy deposition is done: the initial distribution of ionizations in space, which is reflected by the LET, will decide if more or less radicals will escape the spurs, and give more or less molecular products at time 10^{-7} s. The different steps of the non-homogeneous kinetics stage of water radiolysis are summed up in the left part of Fig. 1 (Baldacchino and Katsumura 2010). It is usually when the homogeneous regime is reached (typically between 100 ns and 1 μs) that radical and molecular yields, named *G*-values, are tabulated. They are usually referred to as "primary yields" but yields of formation at shorter time-scale (for example 10 ps after the initial energy deposit)

Table 1 Reaction rates at room temperature in spurs (reactions occurring between 10^{-10} and 10^{-7} s) (Belloni et al. 2008; Buxton et al. 1988)

Reaction	Reaction rate (10^{10} dm³ mol^{-1} s^{-1})
H· + e^-_{aq} + H_2O → OH^- + H_2	2.5
H· + ·OH → H_2O	0.7
H· + H· → H_2	0.78
H_3O^+ + e^-_{aq} → H· + H_2O	2.3
·OH + e^-_{aq} → OH^-	3.0
·OH + ·OH → H_2O_2	0.55
e^-_{aq} + e^-_{aq} + $2H_2O$ → $2OH^-$ + H_2	0.55

Fig. 1 Sketch of reactions of transient species produced by irradiation in pure water (Baldacchino and Katsumura 2010). It includes the secondary electron (e^-_s that is the ejected electron), the thermalized electron (e^-_{th}, whose energy is about 0.025 eV) and the other radicals and molecules described in the text. Axis of time (on the left, vertically), localizations in space (middle, vertically) and LET (top, horizontally) are drawn. The reader is guided from time zero to the homogeneous stage at μs where the values of primary radiolytic yields (*G*-values) are tabulated and shown with respect to the LET axis (from the lowest LET to the highest one). Red arrows indicate the typical variations of *G*-values when LET increases

can be obtained by pulse radiolysis or using the scavenging method (Baldacchino 2008; Schuler et al. 1980). In this case, the time at which *G*-values are given is often clarified through a subscript. Thus, unless otherwise stated, *G*-values correspond to the yields of formation at the beginning of the homogeneous regime and not at time "0". *G*-values are expressed in mol J^{-1} but also in molecule/100 eV in most of the past literature. *G*-value is simply related to the dose and the concentration *C* of the considered species in unit of mol dm^{-3} with a density correction ρ: $C = \rho \times D \times G$. For more details on the water radiolysis model, we invite the reader to consult reference books or reviews. (Le Caer 2011; Farhataziz and Rodgers 1987; Belloni et al. 2008; Baldacchino and Katsumura 2010)
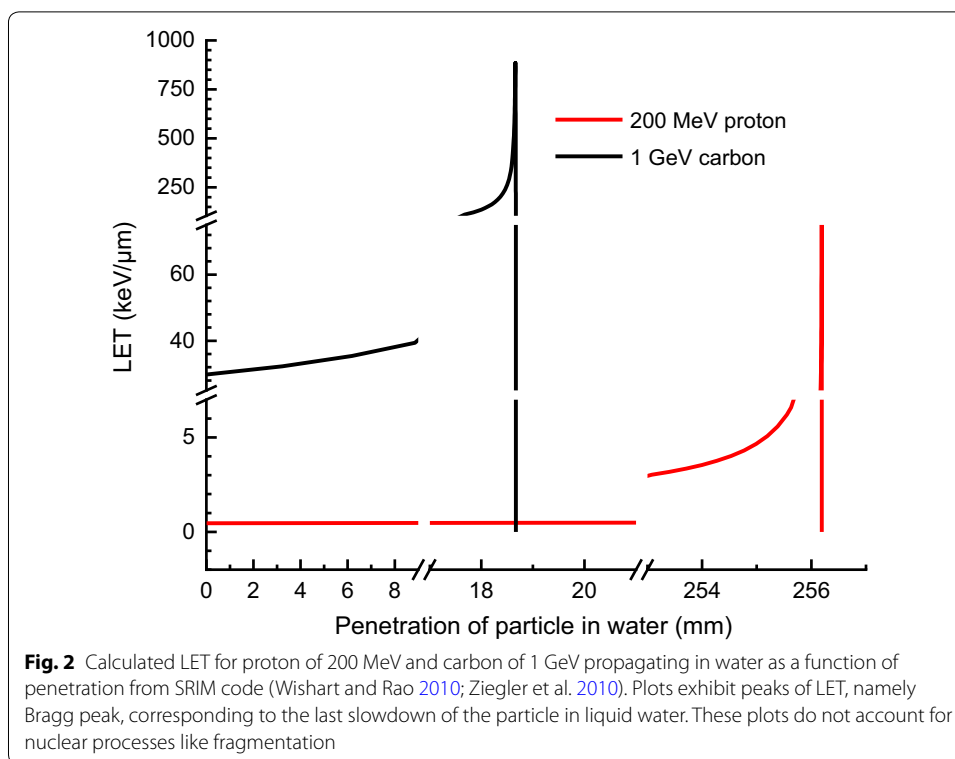
Physico-chemical properties of primary species

As stipulated in Fig. 1, water radiolysis leads to radicals (e^-_{aq}, ·OH, H·, and HO$_2$·) and molecular products (H$_2$, H$_2$O$_2$). They are sometimes referred to as "primary" products but this notion is relative since they all derived from excited and ionized molecules, formed at an earlier stage. They are usually classified into reducing (e^-_{aq}, H·) and oxidizing (·OH, HO$_2$·, H$_2$O$_2$) equivalents. H$_2$ is considered chemically inert and it is often neglected. H$_2$O$^+$ is surely the most reactive oxidant species in water radiolysis but it recombines immediately in the ionization tracks (El Omar et al. 2012; Ma et al. 2018) and, as a strong Brønsted acid, it also deprotonates to form ·OH and hydronium ion (H$_3$O$^+$) within 10^{-13} s. With a longer lifetime, hydroxyl radical, ·OH, is the most

effective oxidant radical towards biological molecules: it has a high standard potential ($E° = 2.34$ V) with respect to Standard Hydrogen Electrode (SHE) at neutral pH. With most substrates, it reacts at nearly diffusion-controlled rates (Buxton et al. 1988). Solvated electron has been the subject of intense research since its first direct detection in 1962 by Hart and Boag (1962). With its conjugate acid (H·, pKa(H·/e^-_{aq}) = 9.1), they are strong reductants ($E°(e^-_{aq}) = -2.9$ V/SHE and $E°(H·) = -2.4$ V/SHE). In many aspects, they behave very similarly but reactions of e^-_{aq} with biomolecules are more documented, both from theoretical (Gu et al. 2012; Kumar et al. 2016) and experimental points of view (Von Sonntag 2006). The latter reports near diffusion-controlled reaction rates of e^-_{aq} with DNA/RNA components and evidence for the reaction of the aqueous electron reaction with dsDNA. Proof of reducible sites in proteins was also given in some experiments (LeTilly et al. 1997). H· and e^-_{aq} are mostly skipped in radiobiology because molecular oxygen competes efficiently to scavenge these species and forms superoxide radical. Given pKa(HO$_2$·/O$_2^-$) = 4.8, O$_2^-$ is the predominant species at physiological pH. More detailed aspects are included in a recent book especially in chapters 13 and 14 (Hatano et al. 2011).

The case of high-LET radiations

Under the name "high-LET" radiations, different types of incident particles are gathered: α particles, protons, heavier ions. Their common denominator is a track-averaged LET higher than a few eV nm^{-1}. For comparison, 1 MeV electrons in water have a "low-LET" of 0.2 eV nm^{-1} (Stopping powers for electrons and positrons 1984). The LET value can be calculated by the Bethe-Bloch equation including ion charge, ionization potential of the target material, etc. Elaborated models can also provide energy distributions around an ion track in more specific conditions if needed [see e.g. (Friedland et al. 2011, 2017; Abril et al. 2015; Garcia-Molina et al. 2009; Nikjoo et al. 2006; Emfietzoglou et al. 2004)]. As mentioned before, for a given particle with defined incident energy, LET is not constant along the track and several formula exist for different energy ranges (Farhataziz and Rodgers 1987), picked up by software such as SRIM to model the whole range of energy deposition of typical ions in a large domain of incident energy (Ziegler et al. 2010). This variation is especially noticeable at the end of the tracks where incident ions are sufficiently slowed down to deposit all their left energy in a small range: this is the Bragg peak region which is illustrated in Fig. 2 for 200 MeV-proton and 1 GeV-carbon ion in water (Ziegler et al. 2010). At the Bragg peak, due to its sharpness, delivered dose can be several 100 times the dose delivered several millimeters before. This is why it is exploited in hadrontherapy: by making spatially coincident the Bragg peak with the tumor, maximal energy deposition in cancerous cells occurs while minimizing damage to healthy tissues. This is especially valuable when the tumor is located close to critical organ structures. Nevertheless, some processes occurring in Bragg peak such as nuclear processes are still misunderstood. Fragmentation of projectile and target can be efficient enough to produce other accelerated light-particles of low-LET having a longer range Maeyama et al. (2011a). This could lead to a diminished protection of healthy tissues and thus must be considered.

The empirical tendency between LET value, track structure and primary yields was drawn by Allen in the 60s (Allen 1961). As high-LET radiation track is densely

Baldacchino *et al. Cancer Nano* (2019) 10:3

Page 6 of 21

Fig. 2 Calculated LET for proton of 200 MeV and carbon of 1 GeV propagating in water as a function of penetration from SRIM code (Wishart and Rao 2010; Ziegler et al. 2010). Plots exhibit peaks of LET, namely Bragg peak, corresponding to the last slowdown of the particle in liquid water. These plots do not account for nuclear processes like fragmentation

Table 2 Primary track-averaged yields for water radiolysis under gamma rays irradiation (LET of 0.23 eV nm^{-1}) and under 12 MeV alpha rays (LET of 108 eV nm^{-1}) in desoxygenated conditions (Belloni et al. 2008; Appleby and Schwarz 1969; Spinks and Woods 1990)

G-values (µmol J^{-1})	e^-_{aq}	H·	·OH	H$_2$	H$_2$O$_2$	H$_3$O$^+$	O$_2^-$/HO$_2$·
Gamma rays (LET of 0.23 eV nm^{-1})	0.28	0.062	0.28	0.047	0.073	0.28	0
12 MeV alpha rays (LET of 108 eV nm^{-1})	0.044	0.028	0.056	0.11	0.11	0.044	0.007

populated with the active species, *G*-values are strongly affected. Primary track-averaged yields are collected in Table 2 for water radiolysis species for comparing low-LET (gamma rays) and high-LET (alpha rays) radiations under deoxygenated conditions.

When increasing LET, molecular species (H$_2$, H$_2$O$_2$) are favored by an intensified recombination of radical species (H·, ·OH and e^-_{aq}) because of the spurs overlapping along the propagation axis of the incident particle. This was observed before the invention of LET formalism: for example, the production of H$_2$ in presence of high-LET particles emitted by fission products was detected in solution by Debierne (1914). Similarly H$_2$O$_2$ production is well-known to be increase by high-LET radiation (Wasselin-Trupin et al. 2002). This situation is similar to the case of a high dose rate, which was recently exploited for therapy (Favaudon et al. 2015; Fouillade et al. 2017). A global view of the localization of events caused by radiation as a function of LET, as well as the evolution of *G*-values with LET, are displayed in the right part of Fig. 1. There is only one exception to this rule, the hydroperoxyl radical/superoxide
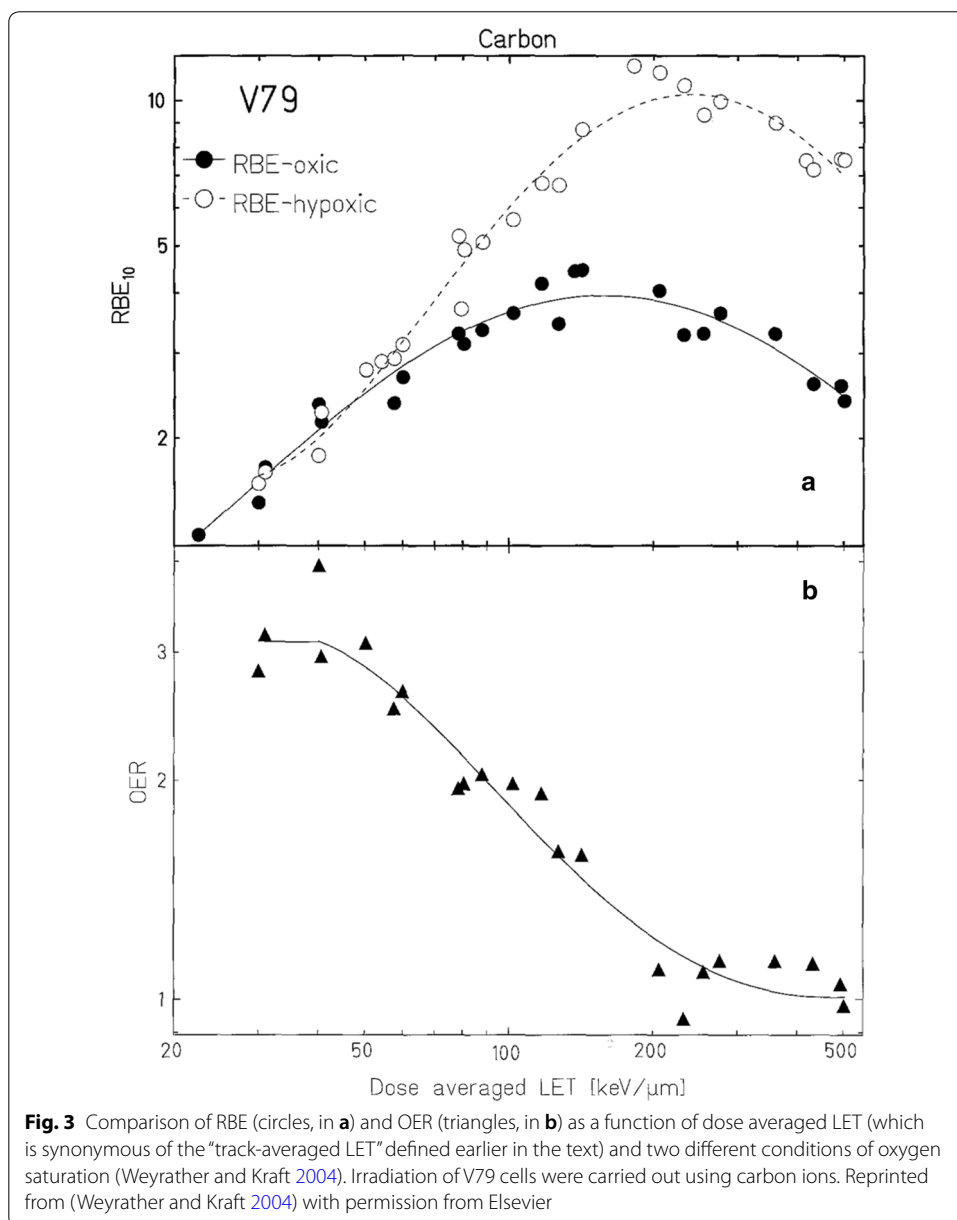
Baldacchino *et al. Cancer Nano* (2019) 10:3

Page 7 of 21

radical ($HO_2\cdot/O_2^-$) couple. The consequences are important as it may bring molecular oxygen in anoxic medium. More details will be brought in the next section.

It is to be noted that for very high-LET particles (above 200 keV μm^{-1}), *G*-values were reported to be higher than expected for radical species, meaning that a significant fraction of radicals can escape from the track (Nikjoo et al. 2001). In these "hard" conditions of radiation, other physical phenomena in relation with the track structure could play an important role in the fate of radical species. Under these conditions a cylindrical volume named "penumbra" formed by a high density of energetic secondary ejected electrons (Magee and Chatterjee 1987) has to be taken into account. These electrons have characteristics of "low-LET" projectiles which could account for these surprisingly high *G*-values. Another possible explanation is the formation of cylindrical shock waves as a result of such a localized and fast energy deposition that could spread radicals out of the ion track and also contribute to direct damages to biomolecules through thermo-mechanical stress (Surdutovich and Solov'yov 2010). But such extreme LET are not widespread.

When it comes to radiobiology, because of the localized energy deposition, complexity of DNA damage is expected to be much greater after high-LET irradiations. Indeed, they have a higher capacity to initiate clustered DNA lesions, called CDD for Complex DNA Damage or LMDS for Locally Multiply Damaged Sites (Sage and Shikazono 2017). All these terms refer to 2 or more damages (single or double-strand breaks, abasic sites, oxidized bases, …) within a 20 base-pair regions, that being so one or two helix turns. This contrasts with the "signature" of most endogenous or exogenous DNA damaging agents that generate relatively isolated and easy-to-repair damages. In addition, the average number of lesions per cluster is predicted to increase with increasing LET: according to simulation, 1 MeV protons (LET 25.4 keV μm^{-1}) generate 1 cluster with 5 lesions for 60 isolated lesions, whereas 4 MeV α particles (LET 105 keV μm^{-1}) generate 1 cluster with 5 lesions for 8 isolated lesions (Nikjoo et al. 2001). Such CDD are more challenging to repair. Recently, Lorat et al. very elegantly showed that low-LET irradiation leads to isolated double-strand breaks randomly distributed throughout the nucleus and nearly all of them are repaired within 24 h while high-LET irradiation produces closely grouped damages that undergo slower and incomplete repair (Lorat et al. 2015). This difficulty in repair translates into the quasi exponential trend of cell survival curves after high-LET irradiation, instead of linear quadratic for low-LET radiation.

To compare the efficiency of different radiations at the cell population level, the relative biological effectiveness (RBE) was introduced. It represents the ratio of the doses needed to observe a given biological effect for a reference and a tested radiation ($RBE = D_{ref}/D_{test}$). As RBE depends on the absorbed dose, the choice and level of the biological observable, the dose rate, the cell line etc. it is incorrect to talk about the RBE of, for example, α-rays versus X-rays without more information. The reference is currently *γ*-rays from ^{60}Co or photons with at least 1 MeV energy (Landberg and Nilsson 2009). A biological endpoint commonly found in literature is 10% of clonogenic survival. Hence the 10 subscript in the following notation. When comparing different radiation types, RBE_{10} slowly increases with LET between 0.1 and 10 eV nm^{-1}, then a steeper slope is observed to reach a maximum for a LET value about 100–200 eV nm^{-1} (Blakely et al. 1984). When carbon ions of different LET are used to irradiate V79 cells, under oxic conditions, the same trend is noticed and the maximum RBE is found

Baldacchino *et al. Cancer Nano*   (2019) 10:3

Page 8 of 21

around 150 keV μm^{-1} [Fig. 3a, black dots (Weyrather and Kraft 2004)]. This can be interpreted as follows: assuming cell death requires the deposit of a certain amount of energy, for low-LET radiations, a single track does not transfer enough energy to reach this threshold. When the LET increases, so does the energy deposited and less trajectories are needed to "kill" the cell, which translates into an increase of RBE. Beyond the maximum, one particle transfers more than the necessary energy. Some energy is "wasted" and the RBE decreases. When comparing different survival levels (1% or 10%) for the same cell line or different cell lines for 10% survival, the position of the maximal RBE does not vary much (Blakely et al. 1984). In other words, high-LET radiations tend to erase the variability of responses between cells, as repair processes play a less prominent role. It is also the case for oxygenation as discussed in the following section.

Fig. 3 Comparison of RBE (circles, in **a**) and OER (triangles, in **b**) as a function of dose averaged LET (which is synonymous of the "track-averaged LET" defined earlier in the text) and two different conditions of oxygen saturation (Weyrather and Kraft 2004). Irradiation of V79 cells were carried out using carbon ions. Reprinted from (Weyrather and Kraft 2004) with permission from Elsevier

Table 3 Reactions that could possibly form O_2 from other reactive oxygen species

Reaction number	Reaction	Rate constant $(M^{-1} s^{-1})$
(1)	$HO_2\cdot + HO_2\cdot \rightarrow H_2O_2 + O_2$	9.7×10^7
(2)	$\cdot OH + HO_2\cdot \rightarrow H_2O + O_2$	6.0×10^9
(3)	$\cdot OH + H_2O_2 \rightarrow H_2O + HO_2\cdot$	2.7×10^7

Rate constants were extracted from reference (Belloni et al. 2008)

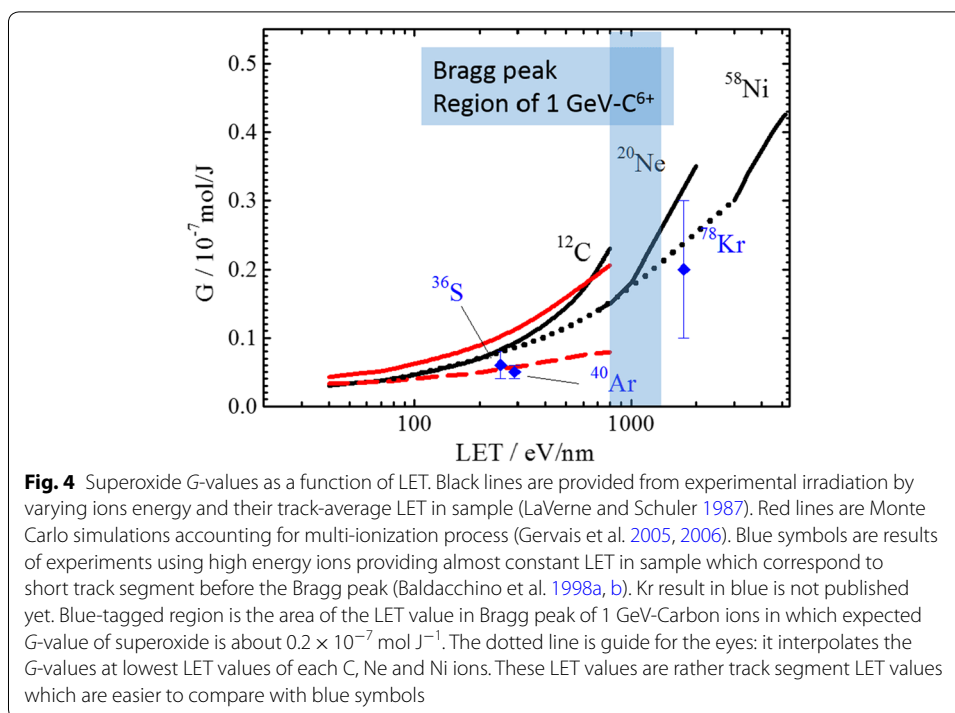## Oxygen effect

Historically, the rationale to develop heavy ions for therapy was not the ballistic properties mentioned above but what is called the "oxygen effect". Nearly a century ago, molecular oxygen was shown to be a crucial component for cell response to irradiation (Crabtree et al. 1933; Rockwell et al. 2009). As early as 1955, Thomlinson and Gray published the first paper suggesting that hypoxia could be a cause for radioresistance (Thomlinson and Gray 1955). O_2 concentration is about 2.5×10^{-4} M under atmospheric pressure in pure water at room temperature, and an average in normal cells is estimated at ca. 30 μM.

As previously mentioned, O_2 scavenges reducing primary species through the fast reactions $O_2 + \cdot H$ ($k = 2.1 \times 10^{10}$ M^{-1} s^{-1}) or $O_2 + e^-_{aq}$ ($k = 1.9 \times 10^{10}$ M^{-1} s^{-1}) to form superoxide radicals. This radical is known not to be very reactive towards biological components: its standard potentials are lower in absolute values than those of HO· and e^-_{aq} (at pH7, $E^{\circ\prime}(O_2^-/H_2O_2) = 0.93$ V and $E^{\circ\prime}(O_2/O_2^-) = -0.33$ V) and it possesses low reaction rate constants. Its toxicity comes from secondary reactions, such as $O_2^- + NO\cdot \rightarrow ONOO^-$ ($k = 1.9 \times 10^{10}$ M^{-1} s^{-1}). The consequence is then the generation of radicals with higher oxidative power, leading to more harmful conditions. Superoxide radical anion toxicity also arises from its capacity to react through iron-catalyzed Haber–Weiss reaction ($O_2^- + H_2O_2 \rightarrow HO^- + HO\cdot + O_2$) leading to HO·. Another process consuming O_2^- is its disproportionation, a fast reaction catalyzed by the superoxide dismutase (SOD) with a 2×10^9 M^{-1} s^{-1} rate constant.

Oxygen is also implicated in radical reactions leading to non-repairable cell component damages. For example, it reacts with carbon-centered radicals, R·, in a nearly diffusion-controlled manner, to produce peroxyl radicals, ROO·, which have a higher reactivity than O_2^- towards proteins, DNA and lipids (Quintiliani 1986; Von Sonntag 1987).

In hypoxic conditions such as those often encountered in tumor cells, one could expect simplified radiolysis reactions due to the absence of oxygen. But surprisingly, in high-LET tracks, O_2 can be formed under anoxic conditions. Where does it come from? One possibility is to create O_2 from other reactive oxygen species like in reactions (1) and (2) in Table 3. Both necessitate $HO_2\cdot$. But in the absence of O_2, there is no efficient pathway to form superoxide or its conjugated acid by scavenging. Another option would be reaction (3) but it appears to be too slow and has almost no chance to occur since faster reactions will take place instead.

Fig. 4 Superoxide *G*-values as a function of LET. Black lines are provided from experimental irradiation by varying ions energy and their track-average LET in sample (LaVerne and Schuler 1987). Red lines are Monte Carlo simulations accounting for multi-ionization process (Gervais et al. 2005, 2006). Blue symbols are results of experiments using high energy ions providing almost constant LET in sample which correspond to short track segment before the Bragg peak (Baldacchino et al. 1998a, b). Kr result in blue is not published yet. Blue-tagged region is the area of the LET value in Bragg peak of 1 GeV-Carbon ions in which expected *G*-value of superoxide is about 0.2×10^{-7} mol J^{-1}. The dotted line is guide for the eyes: it interpolates the *G*-values at lowest LET values of each C, Ne and Ni ions. These LET values are rather track segment LET values which are easier to compare with blue symbols

Yet, clear evidence of $HO_2 \cdot / O_2^-$ formation for high-LET beams were published by LaVerne and Schuler (1987, 1992). For example, we can extract a *G*-value for superoxide of ca. 0.2×10^{-7} mol J^{-1} for 1 GeV C^{6+} (Fig. 4). More recently, Gervais et al. showed that $HO_2 \cdot$ formation is accompanied by O_2 formation, this later predominating at LET higher than 300 eV nm^{-1} (Gervais et al. 2005). As previously suggested, Baldacchino et al. (1998a) simulation approaches confirmed the necessity of multiple water ionizations to produce $HO_2 \cdot$ with high-LET radiation with the following sequence (Gervais et al. 2005; Gaigeot et al. 2007; Meesungnoen and Jay-Gerin 2009):

$$H_2O^{2+} + 2H_2O \rightarrow 2H_3O^+ + O$$

$$O + HO \cdot \rightarrow HO_2 \cdot$$
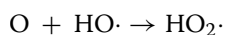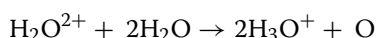
After H^+ transfer to obtain atomic O, $HO_2 \cdot$ can be formed in high-LET tracks and generate O_2 but O_2 formation is not constant over time: for example $^{12}C^{6+}$ ions exhibit a maximum production at 4×10^{-10} s and temporal variation of O_2 production in tracks of heavy ions, from 10^{-12} to 10^{-5} s was calculated by Meesungnoen and Jay-Gerin (2005, 2009). This formation could be correlated to a low pH value ca. 3.3 in tracks, which rapidly increases to 7 after 1 ns (Kanike et al. 2015). The multiple ionization model to explain $HO_2 \cdot$ formation in the track of high-LET radiation and consequently the formation of O_2 in anoxic conditions is currently the most probable model as demonstrated by Meesungnoen and Jay-Gerin in Hatano et al. (2011). Nevertheless, there is no available experimental validation due to the difficulties for monitoring the short lifetime-transient species (Baldacchino 2008).

In case of successive bunches of particles, every new bunch interacts with a biological medium that is richer and richer in oxygen. The high-LET radiation has, therefore, a role

of enrichment in molecular oxygen. Concentration of O_2 produced radiolytically can be three times higher than the averaged concentration of O_2 in normal cells, which could be enough to restore a critical level of damages.

To quantify this impact of oxygen production involved in cell damaging, a parameter, OER for Oxygen Enhancement Ratio, was defined. Very similarly to RBE, it is the ratio of doses needed to observe a given biological effect in hypoxic and normally oxygenated conditions (OER$=D_{hypoxic}/D_{oxic}$). Considering Fig. 3a, when LET is higher than 50 eV nm^{-1}, RBE$_{10}$ differs according to the oxygenation status of the cells: the higher efficiency of high-LET radiation is exacerbated in hypoxic conditions. This is explicitly represented in Fig. 3b where OER as a function of LET is plotted. Nevertheless, for very high-LET, OER is close to 1, which means that the cells oxygenation has no more influence on the cell survival. When LET increases too much, all cellular populations tend to behave more uniformly which could be explained by the presence of too severe damages that the cell cannot repair. In addition, for greater LET than 200 keV μm^{-1}, one knows the ion track exhibits a low-LET radial zone named "penumbra" which can influence the G-values again, for example H_2O_2 G-value reaches a maximum and decreases (Hatano et al. 2011; Wasselin-Trupin et al. 2002).

Experimental physico-chemical approach of radiosensitization by using nanoparticles and high-LET projectiles

Despite their advantageous properties, high-LET radiations are not necessarily the panacea and could be usefully assisted by extrinsic radiosensitizers, such as nanoparticles. In fact, another approach to decrease side effects in normal cells is to deposit higher energy in the tumor by inclusion of metallic nanoparticles. From a physical point of view, it is well established that high-Z elements are more prone to absorb energy than water-equivalent media such as biological tissues and are efficient to eject electrons mainly by Auger cascades when irradiated by low-energy photons. The illustration of such a phenomenon has been highly documented for more than a decade both in vivo and in vitro (Hainfeld et al. 2004) with a majority of studies combining radiation and cellular systems (Rosa et al. 2017). Nevertheless, from this abundant literature, contradictory results emerged, as well as different explanations: for example, even non high-Z elements radiosensitization was evidenced (Grall et al. 2015), and low-energy photons radiation does not seem to be the most efficient to radiosensitize (Brun and Sicard-Roselli 2016). Thus, no consensus could be established to propose an efficient combination of nanoparticle and radiation.

There is no doubt that this phenomenon, whatever its name (radiosensitization, dose enhancement, radiation potentialization…) is the combination of different processes: first, a physical step with energy absorption by the nanoparticle, then a chemical step with radical production and finally biological cascades to induce cell death. According to the radiation type and energy, to the nanoparticle type, shape and coating, and to the cellular localization and internalized quantity, the proportion of each of these steps can highly vary. Anyhow, it is crucial to make a link between these physical, chemical and biological events combining experimental and theoretical approaches. Experimentally, common NP exposures of cells are lower than 100 μg mL^{-1} of metal corresponding to a maximum of a few nM of nanoparticles, depending on their size. Under these
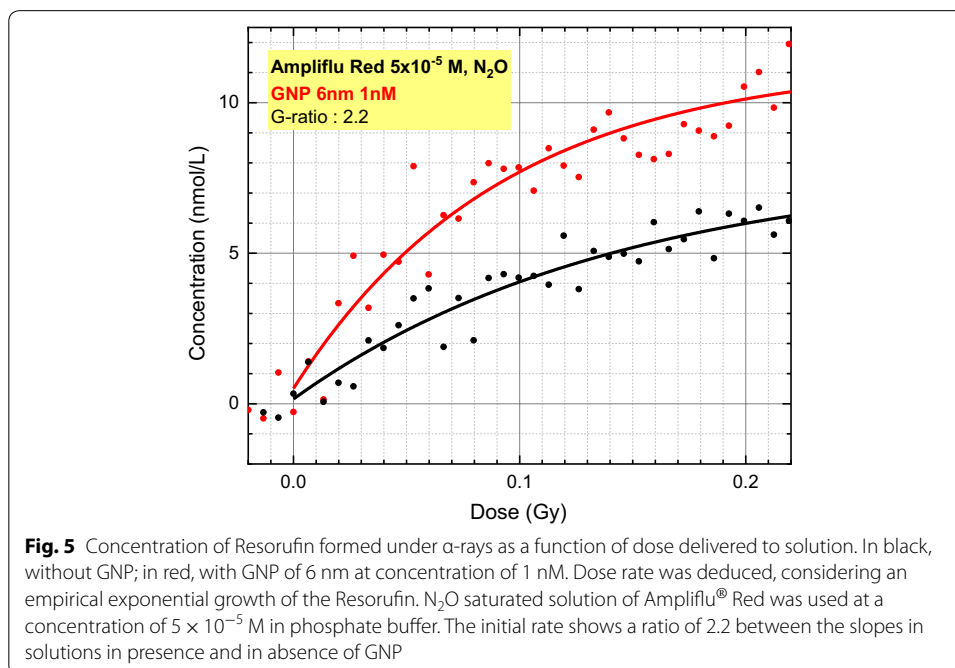
conditions, only a few percents of dose enhancement are expected from the supplementary energy absorption calculated (Gilles et al. 2018). To compare this first physical step to the chemical step, radical quantities need to be determined. Among the few articles presenting experimental measurements of radical overproduction induced by nanoparticles through indirect measurements (Gilles et al. 2018; Misawa and Takahashi 2011; Klein et al. 2012), the maximal G(HO·) reported is four times higher than normal radiolysis, in the absence of oxygen. This difference is now proposed to arise from surface reactions or catalysis at nanoparticle/solvent interface. It should be kept in mind that these radical production measurements implicitly take into account a relation between time and radical production. Indeed, the scavenging processes behind radicals quantification are events temporally defined by reaction rate constants and scavenger concentration. For instance, considering coumarin scavenging, hydroxyl radical production was measured in the range of hundred of nanoseconds considering a concentration of 0.5 mM and $k = 1.05 \times 10^{10}$ M^{-1} s^{-1} (Gilles et al. 2018). When it comes to high-LET radiation, as far as we know, only H$_2$ production at the surface of ZrO$_2$ NP under 5-MeV α-rays was measured (Roth et al. 2012). Even if some cellular studies reported radiosensitization (Kobayashi et al. 2010; Lacombe et al. 2017), radical production has not been experimentally quantified yet. A recent theoretical and numerical study by Haume et al. suggests that the presence of a poly(ethylene glycol) functionalization around 1.6 nm GNP drastically reduces the hydroxyl radicals production when irradiated by carbon ions (Haume et al. 2018). This is in agreement with what was measured with X-rays and larger GNP (Gilles et al. 2018). It is worth mentioning that the initial interaction between gold nanoparticles and high-LET ions must differ from the low-LET as ions have smaller cross-sections for ionization of inner shells of gold (Heredia-Avalos et al. 2007; Solov'yov 2017) but other processes have been considered to contribute to electron emission, especially low-energy electrons, such as plasmon or collective 5d-electrons excitations (Haume et al. 2018).

A dedicated experimental approach is then needed to evaluate effect of high-LET particles as they have a short range in matter, especially considering the Bragg peak region that could have typically a few tens of μm in deepness. Some setups exist for imaging the microdosimetry of alpha rays (Lamart et al. 2017) but do not include time resolution which is necessary to investigate the chemistry in mid-scale of time (i.e. μs-s) and to evaluate the *G*-values of radicals. In this section, such an approach is presented, combining LET effect and the presence of NP to determine the radiolytic yield of radicals with an acquisition of only few seconds. MeV α-particle exposition is one of the available choice for testing LET effect concomitantly to NP. The experimental setup we build considers the μm range of α-particles in dense media and we paid special attention for the sample to be in the Bragg peak region. The fluorescent probe we chose, Ampliflu® Red, allowed an extremely sensitive (Baldacchino et al. 2009; Foley et al. 2005; Maeyama et al. 2011b) in situ and in operando detection without any separation step of molecular products, via chromatography for example. This molecule is known to react with hydrogen peroxide in combination with HRP enzyme and is commonly used to detect oxidant species in microbial systems (Castaño et al. 2018) or under stress conditions (Lefrancois et al. 2016; Kovacik and Babula 2017). This dye and derivatives were also used as chemical dosimeter in proton irradiation (Kim et al. 2007). Its chemical mechanism towards

one-electron oxidation, i.e. formation of resorufin, was recently examined (Debski et al. 2016) showing the diversity of oxidative radicals that could be responsible for such reaction.

Materials and setup details are given in appendix. Briefly, fluorescence of thin liquid sample irradiated from the bottom by a focused α-beam is detected in real-time with a microscope. Fluorescence intensity provided by the formation of resorufin which is excited at 532 nm by a CW laser is proportional to the concentration of ·OH radical, the only species formed by α-radiolysis under our conditions (N_2O degassing). As the concentration (C) of ·OH is related to the dose (D) through G-value, a change in dose rate can be interpreted equivalently to a change in primary G-value. This G-value corresponds to the initial slope of the plot representing the resorufin concentration as a function of the irradiation dose. A typical result is presented in Fig. 5 for a solution of 10^{-5} M of Ampliflu® Red saturated with N_2O to scavenge e^-_{aq} and get a yield value being the sum $G(\cdot OH) + G(e^-_{aq}) = 5.4 \times 10^{-8}$ mol J^{-1} (Lertnaisat et al. 2014). An exponential curve fitting is performed to empirically describe the plotted data and is used for the initial slope determination giving the dose rate value. The exponential shape could result in multiple phenomena including slow chemistry processes leading to the Resorufin formation (Debski et al. 2016) and diffusion processes available at microscopic scale.

Our main interest is the ratio between dose rates obtained with and without GNP to evidence the capacity of alpha radiation to induce radiosensitization through hydroxyl and electron overproduction. Dose rates were determined as it was depicted previously for 1 nM (1.3 μg mL^{-1}) of 6 nm nanoparticles. Our quantification clearly shows supplementary radicals production as the determined ratio is greater than 1 with a value of 2.2 ± 0.5 (see Fig. 5). This preliminary result confirms the enhancement of radiolysis with high-LET radiation. Comparing X- or gamma rays in the same

Fig. 5 Concentration of Resorufin formed under α-rays as a function of dose delivered to solution. In black, without GNP; in red, with GNP of 6 nm at concentration of 1 nM. Dose rate was deduced, considering an empirical exponential growth of the Resorufin. N_2O saturated solution of Ampliflu® Red was used at a concentration of 5×10^{-5} M in phosphate buffer. The initial rate shows a ratio of 2.2 between the slopes in solutions in presence and in absence of GNP

conditions, it appears that α particles are more efficient (unpublished data). This validates our setup and encourages us to conduct more standardized experiments. Indeed, the influence of O_2 could be investigated as its presence reduces radical over-production by a factor of 3 for X-Rays. We also have to develop an accurate determination of dose rate by recording in real-time the α-beam intensity. These results could be interestingly compared to theoretical data. A first milestone was reached as enhancement was predicted by Monte Carlo simulations (McKinnon et al. 2016; Tran et al. 2016) calculated with protons using GEANT4-DNA code (Tran et al. 2016; Lin et al. 2014; Incerti et al. 2016). To observe that phenomenon the authors of these articles varied the distance between the propagation axis of the incident projectile to the NP. Nevertheless, they did not take into account radiolysis processes yet.

To conclude, this preliminary approach could lead to precise yield determination and so information about the chemical processes taking place in the vicinity of nanoparticles under irradiation. Considering that nanoparticles eject electrons locally, the secondary radiolysis could have similar characteristics as high-LET radiation: proximity of reactive species could enhance geminate recombination and molecular species. Then combining high-LET particles and NP could result in very dense deposit of energy, local recombination and probably a major role of oxygen.

Conclusion

High-LET beam modality in radiation therapy is an extraordinary tool for targeting precisely the tumor cells, preserving healthy tissue damages. Valuable radiobiological properties such as an increased RBE and a decreased OER add to this ballistic effect. In this review, we focused on the chemical reactions, especially originating from radiolysis, to explain the LET effect and the in situ production of dioxygen in anoxic environment. This knowledge is essential to interpret radiobiological results obtained after high-LET irradiations. All these processes are space- and time-dependent and cascade during several orders of magnitude of time from 10^{-12} s to seconds.

Our preliminary experiment of quantification of radicals in the presence of small GNP exposed to α-rays showed an enhancement of radiolysis, even with a very low gold concentration of 1.3 µg mL^{-1}. Future investigations will concern the oxygen concentration influence to decipher the chemical processes in the vicinity of GNP. Beyond radical production, the additional modality of bringing NP in tumor cells needs to be more investigated to understand the radiosensitizing mechanisms. Systematic studies must be encouraged, by varying NP parameters (nature, size, concentration) and irradiation conditions (LET, aerobic or anoxic conditions).

Author details
[1] LIDYL, UMR9222 CEA, CNRS, Université Paris-Saclay, 91191 Gif-sur-Yvette Cedex, France. [2] LCP, UMR8000 UPSud, CNRS, Université Paris-Saclay, 91405 Orsay Cedex, France. [3] NIMBE, UMR3685 CEA, CNRS, Université Paris-Saclay, 91191 Gif-sur-Yvette Cedex, France.

Competing interests
The authors declare that they have no competing interests.

Availability of data and materials
Not applicable.

Consent for publication
Not applicable.

Ethics approval and consent to participate
Not applicable.

Appendix

Materials and setup

Solutions and GNP preparation

Ampliflu® Red (*N*-acetyl-3,7-dihydroxyphenoxazine, Sigma Aldrich), also named ADHP or Amplex® Red or A6550, was solubilized at concentrations between 10^{-5} and 2×10^{-4} M in 1 mM phosphate buffer at pH 6.8 in ultra-pure water (Milli-Q, Millipore). Due to the estimated rate constant of 5×10^9 M^{-1} s^{-1} towards ·OH (Debski et al. 2016), a scavenging capacity of 10^6 s^{-1} is expected which means the reaction occurs at the homogeneous stage previously described in Fig. 1. Solutions were prepared on a daily basis. Nitrous oxide (N$_2$O) was bubbled in order to scavenge hydrated electrons and provide additional ·OH (Schuler et al. 1980). In this condition, the observed yield of ·OH is the sum G(·OH) + G(e^-_{aq}). For calibration of fluorescence intensity, Resorufin (7-hydroxy-3*H*-phenoxazin-3-one, Sigma Aldrich) buffered (pH 6.8) stock solutions were prepared at concentrations between 10^{-8} and 10^{-5} M.

Stock solution of gold nanoparticles (GNP) was prepared as proposed by Slot and Geuze (1981). Briefly, 6 nm GNP were synthetized by reducing KAuCl$_4$ solutions (0.125 mM) by a mix of tri-sodium citrate (0.04% m w^{-1} final concentration) and tannic acid (0.05% m w^{-1} final concentration) at 60 °C. Washing was performed by repeated ultracentrifugation cycles and replacement of the supernatant by ultra-pure water (195,000*g*, 40 min, 4 °C, three times). Characterization was realized by transmission electron microscopy (TEM) to determine their size and concentration was calculated based on their plasmon resonance using an absorption coefficient corresponding to their size. A TEM image of these NPs is presented in Fig. 6. GNP size was established at 6.2 ± 0.6 nm by measuring more than 300 objects. GNP concentration in Ampliflu® Red solution in buffer was 0.1 nM.

Fig. 6 Representative TEM image of the 6 nm GNP after washing
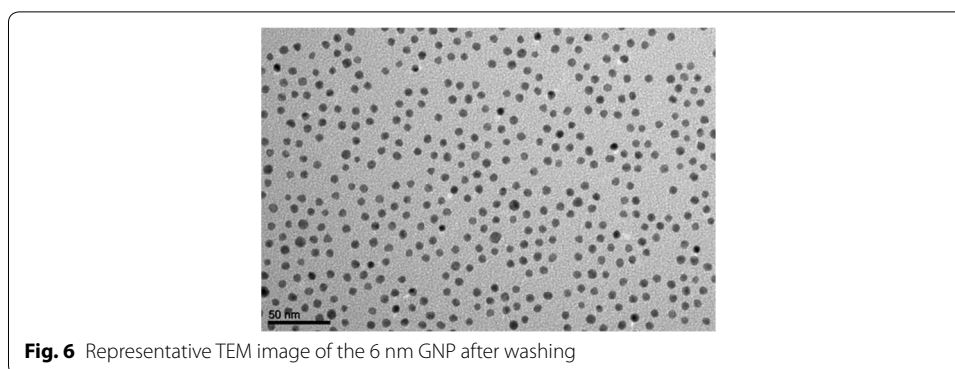
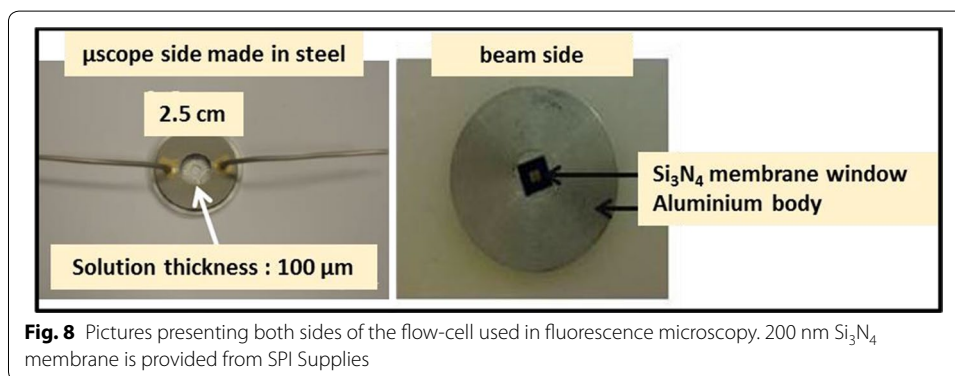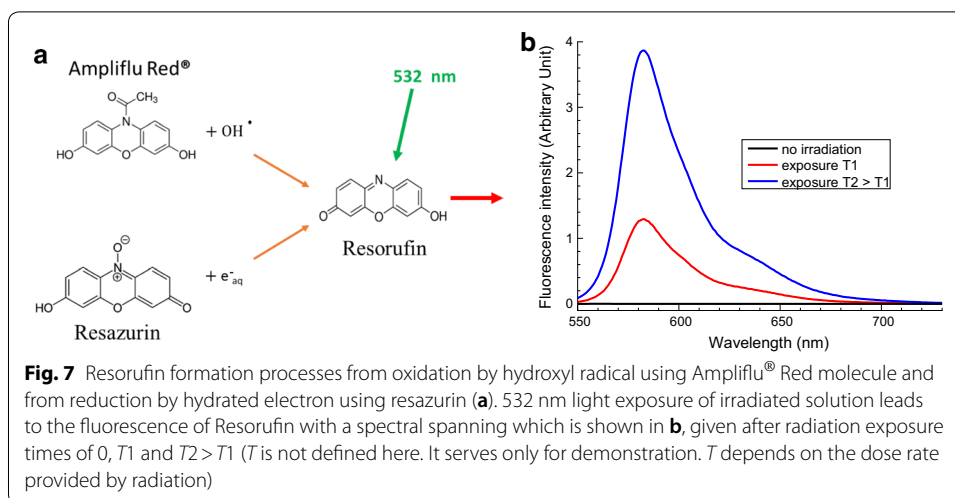### *α-Particle beam and optics for time-resolved fluorescence imaging*

The nuclear microprobe at Saclay, routinely used to investigate solid materials, was used for micro-beam irradiation (Khodja et al. 2009; Khodja 2011). Briefly, the MeV-accelerated light ion beam is vertically extracted to air through a 200 nm-thick Si_3N_4 window that ensures minimal energy loss and spatial straggling. Ion flux, adjustable from 1 to ~4000 ions s^{-1} is regularly monitored by positioning a charged particle detector in front of the exit window. We have estimated the fast fluctuations of the intensity of the beam at about 20%, within 0.1 s. For beam localization, ZnS plate is put in contact with the beam extraction window and fluorescence imaging is carried out with the microscope. One should notice that average LET of the 3-MeV incident α-beam is 130 eV nm^{-1} (calculation from SRIM code). The range of this particle in aqueous solution is about 17 μm which motivated us to construct a very thin chamber in order to observe conveniently the fluorescence light coming from the sample at the Bragg peak of the α-beam.

Sample flow-cell for microscopic imaging in line with micro-beam

Experimental dosimetry was performed by analyzing the fluorescence intensity of the strong emitting molecule Resorufin resulting from the scavenging reactions presented in Fig. 7: reduction (reaction with e^-_{aq}) of Resazurin (Balcerzyk and Baldacchino 2014) or by oxidation (reactions with HO·) of Ampliflu® red (Debski et al. 2016). Only results from the latter reaction are presented in this article.

Determination of radiolytic yields is addressed in a very small volume of solution under very low intensity of α-rays. As previously mentioned, 3-MeV α-particles are delivered by the α-accelerator at a rate of few thousands of ions per second on a section of a few $μm^2$. The method consists in putting in contact a reactor vessel with the beam exit window. Beam induced fluorescence is then observed with a coaxial microscope (BX41, Olympus). The continuous micro-beam irradiates from the bottom, a homemade ultrathin flow-through optical cell namely the reactor vessel presented in Fig. 8. The liquid solution is pushed by a syringe pump (Asia pump by SYRRIS). It can flow in a 0.1 mm thickness chamber between a Si_3N_4 window of 200 nm of thickness which is crossed by the energetic projectiles, and a 0.1 mm of high precision microscope cover glass window on the observation side of the microscope optics. A flow of about 1 cm^3 min^{-1} allows the

Fig. 7 Resorufin formation processes from oxidation by hydroxyl radical using Ampliflu® Red molecule and from reduction by hydrated electron using resazurin (**a**). 532 nm light exposure of irradiated solution leads to the fluorescence of Resorufin with a spectral spanning which is shown in **b**, given after radiation exposure times of 0, *T*1 and *T*2 > *T*1 (*T* is not defined here. It serves only for demonstration. *T* depends on the dose rate provided by radiation)

Fig. 8 Pictures presenting both sides of the flow-cell used in fluorescence microscopy. 200 nm Si_3N_4 membrane is provided from SPI Supplies
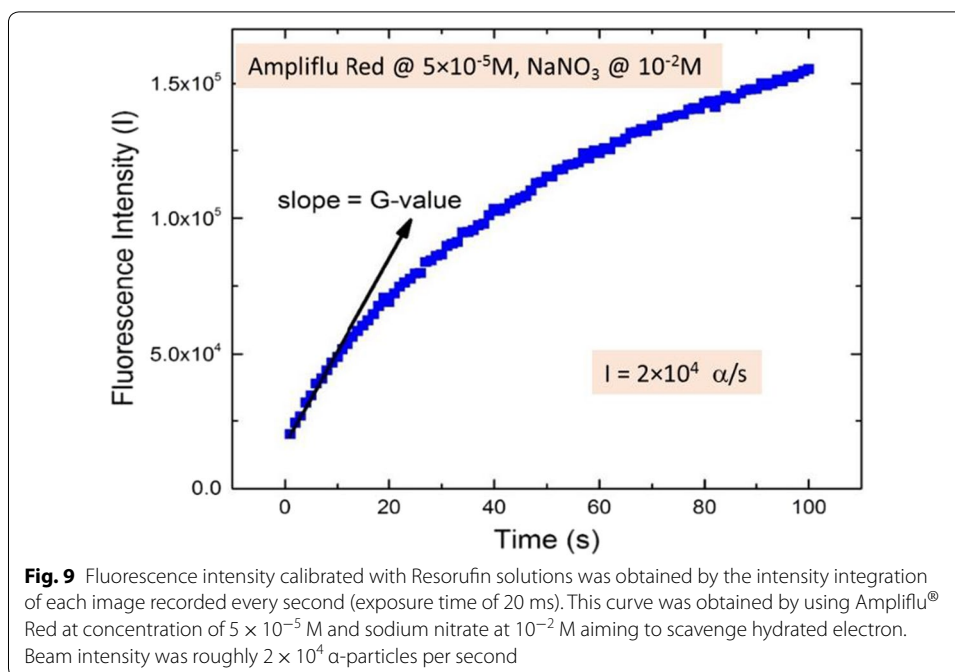
renewing of the solution in a few seconds between 2 experiments. Excitation light provided by an attenuated 200 mW DPPS laser at 532 nm (Laserboxx, OXXIUS) is injected in the microscope using a dichroic mirror and focused in the sample through this latter window. Fluorescence from the irradiated solution is collected by a 10× objective aligned with the α-beam. This light is filtered using OG570 long pass filter and the detection is made by an intensified CCD camera (PiMax3, Princeton Instruments). Image collection is carried out at regular time intervals by using a pulse generator (1 Hz repetition rate, 20 ms exposure time). An optical shutter is closed to avoid solution illumination between 2 expositions.

Data treatment to quantify dose rate

In Fig. 9, fluorescence intensity plotted as a function of time is obtained from the images integrated every second. It is interpreted as the formation of Resorufin formation during irradiation. Fluorescence intensity is proportional to its concentration and time is proportional to the dose. As a consequence, the initial slope of the plot reflects the primary yield of ·OH at a µs scavenging time range. Yields of formation of hydroxyl radical should be determined with the initial slope of the fluorescence intensity build-up, within a few seconds. An application of this method is proposed here

Fig. 9 Fluorescence intensity calibrated with Resorufin solutions was obtained by the intensity integration of each image recorded every second (exposure time of 20 ms). This curve was obtained by using Ampliflu® Red at concentration of 5×10^{-5} M and sodium nitrate at 10^{-2} M aiming to scavenge hydrated electron. Beam intensity was roughly 2×10^4 α-particles per second

in the context of radiosensibilization by combining high-LET α-rays and GNP solution. We considered here that there is no energy transfer between the excited state of Resorufin and NP considering the low thickness of the sample and the low concentration of NP (a few nM). In this way, we can use comparison of slope values for addressing exclusively the enhancement ratio in presence or not of NP. The determination of *G*-values will be addressed in a future study. Nevertheless to calibrate radical production by α-rays we decided to use a yield evaluation presented in literature for α-rays of similar energy (Lertnaisat et al. 2014) where authors found a primary yield of 2.7×10^{-8} mol J^{-1} for ·OH and e^-_{aq}.

Publisher's Note

References

Abril I, de Vera P, Garcia-Molina R, Kyriakou I, Emfietzoglou D. Lateral spread of dose distribution by therapeutic proton beams in liquid water. Nucl Instrum Methods Phys Res Sect B Beam Interact Mater Atoms. 2015;352:176–80. https://doi.org/10.1016/j.nimb.2014.11.100.

Allen AO. The radiation chemistry of water and aqueous solutions. Princeton: D. Van Nostrand; 1961.

Appleby A, Schwarz HA. Radical and molecular yields in water irradiated by.gamma.-rays and heavy ions. J Phys Chem. 1969;73(6):1937–41. https://doi.org/10.1021/j100726a048.

Balcerzyk A, Baldacchino G. Implementation of laser induced fluorescence in a pulse radiolysis experiment—a new way to analyze resazurin-like reduction mechanisms. Analyst. 2014;139:1707–12. https://doi.org/10.1039/c3an02000b.

Baldacchino G. Pulse radiolysis in water with heavy-ion beams. A short review. Radiat Phys Chem. 2008;77(10–12):1218–23. https://doi.org/10.1016/j.radphyschem.2008.05.033.

Baldacchino G. L'apport des ions accélérés dans l'épopée de la chimie sous rayonnement. In: CNRS, editor. Histoire de la Recherche Contemporaine, vol VI. vol 1. 2017. p. 47–55.

Baldacchino G, Katsumura Y. Chemical processes in heavy ions track. In: Rao BSM, Wishart JF, editors. Recent trends in radiation chemistry. Singapore: World Scientific Publishing Co. Pte. Ltd.; 2010. p. 231–54.

Baldacchino G, Le Parc D, Hickel B, Gardes-Albert M, Abedinzadeh Z, Jore D, Deycard S, Bouffard S, Mouton V, Balanzat E. Direct observation of HO_2/O_2^- free radicals generated in water by a high-linear energy transfer pulsed heavy-ion beam. Radiat Res. 1998a;149(2):128–33.

Baldacchino G, Bouffard S, Balanzat E, Gardes-Albert M, Abedinzadeh Z, Jore D, Deycard S, Hickel B. Direct time-resolved measurement of radical species formed in water by heavy ions irradiation. Nucl Instrum Methods Physics Res Sect B Beam Interact Mater Atoms. 1998b;146(1–4):528–32.

Baldacchino G, Maeyama T, Yamashita S, Taguchi M, Kimura A, Katsumura Y, Murakami T. Determination of the time-dependent OH-yield by using fluorescent probe. Application to heavy ion irradiation. Chem Phys Lett. 2009;468(4–6):275–9. https://doi.org/10.1016/j.cplett.2008.12.006.

Belloni J, Mostafavi M, Douki T, Spotheim-Maurizot M. Radiation chemistry—from basics to applications in material and life sciences. Actual Chim. 2008;316:I–XX.

Blakely EA, Ngo FQH, Curtis SB, Tobias CA. Heavy-ion radiobiology: cellular studies. In: Lett JT, editor. Advances in radiation biology, vol. 11. Amsterdam: Elsevier; 1984. p. 295–389. https://doi.org/10.1016/b978-0-12-035411-5.50013-7.

Brun E, Sicard-Roselli C. Actual questions raised by nanoparticle radiosensitization. Radiat Phys Chem. 2016;128:134–42. https://doi.org/10.1016/j.radphyschem.2016.05.024.

Buxton GV, Greenstock CL, Helman WP, Ross AB. Critical-review of rate constants for reactions of hydrated electrons, hydrogen-atoms and hydroxyl radicals ($\cdot OH/\cdot O^-$) in aqueous-solution. J Phys Chem Ref Data. 1988;17(2):513–886.

Castaño JD, Zhang J, Schilling JS. Evaluation of colorimetric assays for determination of H_2O_2 in planta during fungal wood decomposition. J Microbiol Methods. 2018;145:10–3. https://doi.org/10.1016/j.mimet.2017.12.004.

Crabtree HG, Cramer W, Murray James A. The action of radium on cancer cells. II.—some factors determining the susceptibility of cancer cells to radium. Proc R Soc Lond Ser B Contain Pap Biol Character. 1933;113(782):238–50. https://doi.org/10.1098/rspb.1933.0044.

Debierne A. Recherches sur les gaz produits par les substances radioactives. Décomposition de l'eau. Annales de Physique. 1914;2:97–127.

Debski D, Smulik R, Zielonka J, Michalowski B, Jakubowska M, Debowska K, Adamus J, Marcinek A, Kalyanaraman B, Sikora A. Mechanism of oxidative conversion of Amplex (R) Red to resorufin: pulse radiolysis and enzymatic studies. Free Radic Biol Med. 2016;95:323–32. https://doi.org/10.1016/j.freeradbiomed.2016.03.027.

El Omar AK, Schmidhammer U, Rousseau B, LaVerne J, Mostafavi M. Competition reactions of $H_2O^{\cdot+}$ radical in concentrated Cl^- aqueous solutions: picosecond pulse radiolysis study. J Phys Chem A. 2012;116(47):11509–18. https://doi.org/10.1021/jp309381z.

Emfietzoglou D, Karava K, Papamichael G, Moscovitch M. Monte-Carlo calculations of radial dose and restricted-let for protons in water. Radiat Prot Dosimetry. 2004;110(1–4):871–9. https://doi.org/10.1093/rpd/nch163.

Farhataziz RMAJ, Rodgers MAJ. Radiation chemistry—principles and applications. New York: VCH Publishers; 1987.

Favaudon V, Fouillade C, Vozenin MC. Ultrahigh dose-rate, "flash" irradiation minimizes the side-effects of radiotherapy. Cancer Radiother. 2015;19(6–7):526–31. https://doi.org/10.1016/j.canrad.2015.04.006.

Ferradini C, Jay-Gerin JP. Radiolysis of water and aqueous solutions—history and present state of the science. Can J Chem Revue Canadienne De Chimie. 1999;77(9):1542–75.

Foley S, Rotureau P, Pin S, Baldacchino G, Renault JP, Mialocq JC. Radiolysis of confined water: production and reactivity of hydroxyl radicals. Angew Chem Int Ed Engl. 2005;44(1):110–2. https://doi.org/10.1002/anie.200460284.

Fouillade C, Favaudon V, Vozenin MC, Romeo PH, Bourhis J, Verrelle P, Devauchelle P, Patriarca A, Heinrich S, Mazal A, Dutreix M. Hopes of high dose-rate radiotherapy. Bull Cancer. 2017;104(4):380–4. https://doi.org/10.1016/j.bulcan.2017.01.012.

Friedland W, Dingfelder M, Kundrát P, Jacob P. Track structures, DNA targets and radiation effects in the biophysical Monte Carlo simulation code PARTRAC. Mutat Res Fundam Mol Mech Mutagen. 2011;711(1–2):28–40. https://doi.org/10.1016/j.mrfmmm.2011.01.003.

Friedland W, Schmitt E, Kundrat P, Dingfelder M, Baiocco G, Barbieri S, Ottolenghi A. Comprehensive track-structure based evaluation of DNA damage by light ions from radiotherapy-relevant energies down to stopping. Sci Rep. 2017;7:15. https://doi.org/10.1038/srep45161.

Gaigeot MP, Vuilleumier R, Stia C, Galassi ME, Rivarola R, Gervais B, Politis MF. A multi-scale ab initio theoretical study of the production of free radicals in swift ion tracks in liquid water. J Phys B Atom Mol Opt Phys. 2007;40(1):1–12. https://doi.org/10.1088/0953-4075/40/1/001.

Garcia-Molina R, Abril I, Denton CD, Heredia-Avalos S, Kyriakou I, Emfietzoglou D. Calculated depth-dose distributions for H+ and He+ beams in liquid water. Nucl Instrum Methods Phys Res Sect B. 2009;267(16):2647–52. https://doi.org/10.1016/j.nimb.2009.05.038.

Gervais B, Beuve M, Olivera GH, Galassi ME, Rivarola RD. Production of HO_2 and O_2 by multiple ionization in water radiolysis by swift carbon ions. Chem Phys Lett. 2005;410(4–6):330–4. https://doi.org/10.1016/j.cplett.2005.05.057.

Gervais B, Beuve M, Olivera GH, Galassi ME. Numerical simulation of multiple ionization and high LET effects in liquid water radiolysis. Radiat Phys Chem. 2006;75(4):493–513. https://doi.org/10.1016/j.radphyschem.2005.09.015.

Giesel FO. Ueber radium und radioactive Stoffe. Ber Dtsch Chem Ges. 1902;35(3):3608–11.

Gilles M, Brun E, Sicard-Roselli C. Quantification of hydroxyl radicals and solvated electrons produced by irradiated gold nanoparticles suggests a crucial role of interfacial water. J Colloid Interface Sci. 2018;525:31–8. https://doi.org/10.1016/j.jcis.2018.04.017.

Grall R, Girard H, Saad L, Petit T, Gesset C, Combis-Schlumberger M, Paget V, Delic J, Arnault J-C, Chevillard S. Impairing the radioresistance of cancer cells by hydrogenated nanodiamonds. Biomaterials. 2015;61:290–8. https://doi.org/10.1016/j.biomaterials.2015.05.034.

Gu J, Leszczynski J, Schaefer HF. Interactions of electrons with bare and hydrated biomolecules: from nucleic acid bases to DNA segments. Chem Rev. 2012;112(11):5603–40. https://doi.org/10.1021/cr3000219.

Hainfeld JF, Slatkin DN, Smilowitz HM. The use of gold nanoparticles to enhance radiotherapy in mice. Phys Med Biol. 2004;49(18):N309–15. https://doi.org/10.1088/0031-9155/49/18/n03.

Hart EJ, Boag JW. Absorption spectrum of the hydrated electron in water and in aqueous solutions. J Am Chem Soc. 1962;84(21):4090–5. https://doi.org/10.1021/ja00880a025.

Hatano Y, Katsumura Y, Mozumder A, editors. Charged particle and photon interactions with matter. Recent advances, applications, and interfaces. Boca Raton: CRC Press, Taylor and Francis Group; 2011.

Haume K, de Vera P, Verkhovtsev A, Surdutovich E, Mason NJ, Solov'yov AV. Transport of secondary electrons through coatings of ion-irradiated metallic nanoparticles. Eur Phys J D. 2018;72(6):22. https://doi.org/10.1140/epjd/e2018-90050-x.

Heredia-Avalos S, Abril I, Denton CD, Moreno-Marin JC, Garcia-Molina R. Target inner-shells contributions to the stopping power and straggling for H and He ions in gold. J Phys Condens Matter. 2007;19(46):8. https://doi.org/10.1088/0953-8984/19/46/466205.

Incerti S, Douglass M, Penfold S, Guatelli S, Bezak E. Review of Geant4-DNA applications for micro and nanoscale simulations. Phys Med. 2016;32(10):1187–200. https://doi.org/10.1016/j.ejmp.2016.09.007.

Jonah CD. A short history of the radiation chemistry of water. Radiat Res. 1995;144(2):141–7. https://doi.org/10.2307/3579253.

Kanike V, Meesungnoen J, Jay-Gerin JP. Acid spike effect in spurs/tracks of the low/high linear energy transfer radiolysis of water: potential implications for radiobiology. RSC Adv. 2015;5(54):43361–70. https://doi.org/10.1039/c5ra07173a.

Kernbaum M. Sur la d'ecomposition de l'eau par les rayons β du radium et par les rayons ultra-violets. Le Radium. 1909;6(8):225–8.

Khodja H. Ion microbeam irradiation for radiobiology and radical chemistry: status and prospect. In: J Phys Conf Series, vol. 261, no. 1. 2011. p. 012012.

Khodja H, Hanot M, Carriere M, Hoarau J, Angulo JF. The single-particle microbeam facility at CEA-Saclay. Nucl Instrum Methods Phys Res Sect B Beam Interact Mater Atoms. 2009;267(12–13):1999–2002. https://doi.org/10.1016/j.nimb.2009.03.040.

Kim MJ, Pal S, Tak YK, Lee K-H, Yang TK, Lee S-J, Song JM. Determination of the dose-depth distribution of proton beam using resazurin assay in vitro and diode laser-induced fluorescence detection. Anal Chim Acta. 2007;593(2):214–23. https://doi.org/10.1016/j.aca.2007.05.009.

Klein S, Sommer A, Distel LVR, Neuhuber W, Kryschi C. Superparamagnetic iron oxide nanoparticles as radiosensitizer via enhanced reactive oxygen species formation. Biochem Biophys Res Commun. 2012;425(2):393–7. https://doi.org/10.1016/j.bbrc.2012.07.108.

Kobayashi K, Usami N, Porcel E, Lacombe S, Le Sech C. Enhancement of radiation effect by heavy elements. Mutat Res. 2010;704(1):123–31. https://doi.org/10.1016/j.mrrev.2010.01.002.

Kovacik J, Babula P. Fluorescence microscopy as a tool for visualization of metal-induced oxidative stress in plants. Acta Physiol Plant. 2017;39(8):7. https://doi.org/10.1007/s11738-017-2455-0.

Kroh J, editor. Early developments in radiation chemistry. Cambridge: The Royal Society of Chemistry; 1989.

Kumar A, Adhikary A, Shamoun L, Sevilla MD. Do solvated electrons (e^-_{aq}) reduce DNA bases? A Gaussian 4 and density functional theory-molecular dynamics study. J Phys Chem B. 2016;120(9):2115–23. https://doi.org/10.1021/acs.jpcb.5b11269.

Lacombe S, Porcel E, Scifoni E. Particle therapy and nanomedicine: state of art and research perspectives. Cancer Nanotechnol. 2017;8(1):9. https://doi.org/10.1186/s12645-017-0029-x.

Lamart S, Miller BW, Van der Meeren A, Tazrart A, Angulo JF, Griffiths NM. Actinide bioimaging in tissues: comparison of emulsion and solid track autoradiography techniques with the iQID camera. PLoS ONE. 2017;12(10):18. https://doi.org/10.1371/journal.pone.0186370.

Landberg T, Nilsson P. Prescribing, recording, and reporting external beam therapy a summary of ICRU Reports nos 29, 50, 62 and 71. In: Adliene D, editor. Medical physics in the Baltic States: proceedings of the 7th international conference on medical physics. Kaunas: Kaunas Univ Technology Press; 2009. p. 43.

LaVerne JA, Schuler RH. Track effects in radiation chemistry: production of hydroperoxy radical in the radiolysis of water by high-LET nickel-58 ions. J Phys Chem. 1987;91(26):6560–3. https://doi.org/10.1021/j100310a028.

LaVerne JA, Schuler RH. Track effects in the radiolysis of water—$HO_2\cdot$ production by 200–800-MeV carbon-ions. J Phys Chem. 1992;96(18):7376–8. https://doi.org/10.1021/j100197a044.

Le Caer S. Water radiolysis: influence of oxide surfaces on H2 production under ionizing radiation. Water. 2011;3(1):235–53. https://doi.org/10.3390/w3010235.

Lefrancois P, Vajrala VSR, Arredondo IB, Goudeau B, Doneux T, Bouffier L, Arbault S. Direct oxidative pathway from amplex red to resorufin revealed by in situ confocal imaging. Phys Chem Chem Phys. 2016;18(37):25817–22. https://doi.org/10.1039/c6cp04438g.

Lertnaisat P, Katsumura Y, Mukai S, Umehara R, Shimizu Y, Suzuki M. Simulation of the inhibition of water alpha-radiolysis via H_2 addition. J Nucl Sci Technol. 2014;51(9):1087–95. https://doi.org/10.1080/00223131.2014.907548.

LeTilly V, Pin S, Hickel B, Alpert B. Pulse radiolysis reduction of myoglobin. Hydrated electrons diffusion inside the protein matrix. J Am Chem Soc. 1997;119(44):10810–4. https://doi.org/10.1021/ja9635591.

Lin YT, McMahon SJ, Scarpelli M, Paganetti H, Schuemann J. Comparing gold nano-particle enhanced radiotherapy with protons, megavoltage photons and kilovoltage photons: a Monte Carlo simulation. Phys Med Biol. 2014;59(24):7675–89. https://doi.org/10.1088/0031-9155/59/24/7675.

Lorat Y, Brunner CU, Schanz S, Jakob B, Taucher-Scholz G, Rübe CE. Nanoscale analysis of clustered DNA damage after high-LET irradiation by quantitative electron microscopy—the heavy burden to repair. DNA Repair. 2015;28:93–106. https://doi.org/10.1016/j.dnarep.2015.01.007.

Ma J, Wang FR, Mostafavi M. Ultrafast chemistry of water radical cation, H_2O^{-+}, in aqueous solutions. Molecules. 2018;23(2):15. https://doi.org/10.3390/molecules23020244.

Maeyama T, Yamashita S, Taguchi M, Baldacchino G, Sihver L, Murakami T, Katsumura Y. Production of a fluorescence probe in ion-beam radiolysis of aqueous coumarin-3-carboxylic acid solution-2: effects of nuclear fragmentation and its simulation with PHITS. Radiat Phys Chem. 2011a;80(12):1352–7. https://doi.org/10.1016/j.radphyschem.2011.07.004.

Maeyama T, Yamashita S, Baldacchino G, Taguchi M, Kimura A, Murakami T, Katsumura Y. Production of a fluorescence probe in ion-beam radiolysis of aqueous coumarin-3-carboxylic acid solution-1: beam quality and concentration dependences. Radiat Phys Chem. 2011b;80(4):535–9. https://doi.org/10.1016/j.radphyschem.2010.11.013.

Magee JL. Introduction: Milton Burton, Godfather of radiation chemistry 4 March 1902–10 November 1985. Int J Radiat Appl Instrum Part C Radiat Phys Chem. 1988;32(1):1–2. https://doi.org/10.1016/1359-0197(88)90004-5.

Magee JL, Chatterjee A. Track reactions of radiation chemistrty. In: Freeman GR, editor. Kinetics of nonhomogenoeous processes. a practical introduction for chemists, biologists, physicists, and materials scientists. New york: Wiley; 1987. p. 171–214.

McKinnon S, Guatelli S, Incerti S, Ivanchenko V, Konstantinov K, Corde S, Lerch M, Tehei M, Rosenfeld A. Local dose enhancement of proton therapy by ceramic oxide nanoparticles investigated with Geant4 simulations. Phys Med. 2016;32(12):1584–93. https://doi.org/10.1016/j.ejmp.2016.11.112.

Meesungnoen J, Jay-Gerin JP. Effect of multiple ionization on the yield of H_2O_2 produced in the radiolysis of aqueous 0.4 M H_2SO_4 solutions by high-LET $^{12}C^{6+}$ and $^{20}Ne^{9+}$ ions. Radiat Res. 2005;164(5):688–94.

Meesungnoen J, Jay-Gerin JP. High-LET ion radiolysis of water: oxygen production in tracks. Radiat Res. 2009;171(3):379–86.

Misawa M, Takahashi J. Generation of reactive oxygen species induced by gold nanoparticles under x-ray and UV irradiations. Nanomed Nanotechnol Biol Med. 2011;7(5):604–14. https://doi.org/10.1016/j.nano.2011.01.014.

News of Science (1957). Science 125(3236):18–22. https://doi.org/10.1126/science.125.3236.18.

Nikjoo H, O'Neill P, Wilson WE, Goodhead DT. Computational approach for determining the spectrum of DNA damage induced by ionizing radiation. Radiat Res. 2001;156(5):577–83. https://doi.org/10.1667/0033-7587(2001)156%5b0577:CAFDTS%5d2.0.CO;2.

Nikjoo H, Uehara S, Emfietzoglou D, Cucinotta FA. Track-structure codes in radiation research. Radiat Meas. 2006;41(9–10):1052–74. https://doi.org/10.1016/j.radmeas.2006.02.001.

Quintiliani M. The oxygen effect in radiation inactivation of DNA and enzymes. Int J Radiat Biol Relat Stud Phys Chem Med. 1986;50(4):573–94. https://doi.org/10.1080/09553008614550981.

Rockwell S, Dobrucki IT, Kim EY, Marrison ST, Vu VT. Hypoxia and radiation therapy: past history, ongoing research, and future promise. Curr Mol Med. 2009;9(4):442–58.

Rosa S, Connolly C, Schettino G, Butterworth KT, Prise KM. Biological mechanisms of gold nanoparticle radiosensitization. Cancer Nanotechnol. 2017;8(1):2. https://doi.org/10.1186/s12645-017-0026-0.

Roth O, Dahlgren B, LaVerne JA. Radiolysis of water on ZrO_2 nanoparticles. J Phys Chem C. 2012;116(33):17619–24. https://doi.org/10.1021/jp304237c.

Sage E, Shikazono N. Radiation-induced clustered DNA lesions: repair and mutagenesis. Free Radic Biol Med. 2017;107:125–35. https://doi.org/10.1016/j.freeradbiomed.2016.12.008.

Schuler RH, Patterson LK, Janata E. Yield for the scavenging of OH radicals in the radiolysis of N_2O-saturated aqueous-solutions. J Phys Chem. 1980;84(16):2088–9. https://doi.org/10.1021/j100453a020.

Slot JW, Geuze HJ. Sizing of protein A-colloidal gold probes for immunoelectron microscopy. J Cell Biol. 1981;90:533–6.

Solov'yov AV. Nanoscale insights into ion-beam cancer therapy. Switzerland: Springer International Publishing; 2017. https://doi.org/10.1007/978-3-319-43030-0.

Spinks JWT, Woods RJ. An introduction to radiation chemitry. 3rd ed. New York: Wiley; 1990.

Stopping powers for electrons and positrons. ICRU Report, vol 37. Bethesda: International Commission on radiation Units and Measurements; 1984.

Surdutovich E, Solov'yov AV. Shock wave initiated by an ion passing through liquid water. Phys Rev E. 2010;82(5):5. https://doi.org/10.1103/PhysRevE.82.051915.

Thomlinson RH, Gray LH. The histological structure of some human lung cancers and the possible implications for radiotherapy. Br J Cancer. 1955;9(4):539–49.

Tran HN, Karamitros M, Ivanchenko VN, Guatelli S, McKinnon S, Murakami K, Sasaki T, Okada S, Bordage MC, Francis Z, El Bitar Z, Bernal MA, Shin JI, Lee SB, Barberet P, Tran TT, Brown JMC, Hao TVN, Incerti S. Geant4 Monte Carlo simulation of absorbed dose and radiolysis yields enhancement from a gold nanoparticle under MeV proton irradiation. Nucl Instrum Methods Phys Res Sect B Beam Interact Mater Atoms. 2016;373:126–39. https://doi.org/10.1016/j.nimb.2016.01.017.

Von Sonntag C. The chemical basis of radiation biology. New York: Taylor and Francis; 1987.

Von Sonntag C. Free-radical-induced DNA damage and its repair. A chemical perspective. Berlin: Springer; 2006. https://doi.org/10.1007/3-540-30592-0.

Wasselin-Trupin V, Baldacchino G, Bouffard S, Hickel B. Hydrogen peroxide yields in water radiolysis by high-energy ion beams at constant LET. Radiat Phys Chem. 2002;65(1):53–61.

Weyrather WK, Kraft G. RBE of carbon ions: experimental data and the strategy of RBE calculation for treatment planning. Radiother Oncol. 2004;73:S161–9. https://doi.org/10.1016/S0167-8140(04)80041-0.

Wishart JF, Rao BSM. Recent trends in radiation chemistry. Singapore: World Scientific Publishing Co. Pte. Ltd.; 2010.

Ziegler JF, Ziegler MD, Biersack JP. SRIM—The stopping and range of ions in matter (2010). Nucl Instrum Methods Phys Res Sect B Beam Interact Mater Atoms. 2010;268(11–12):1818–23. https://doi.org/10.1016/j.nimb.2010.02.091.

Zimbrick JD. Radiation chemistry and the radiation research society: a history from the beginning. Radiat Res. 2002;158(2):127–40. https://doi.org/10.1667/0033-7587(2002)158%5b0127:RRSRCA%5d2.0.CO;2.